Deconvolution of Thomson scattering temperature profiles

R. Scannell,[1,a)] M. Beurskens,[1] P. G. Carolan,[1] A. Kirk,[1] M. Walsh,[1,b)] T. O'Gorman,[2] and T. H. Osborne[3]
[1]*EURATOM/CCFE Fusion Association, Culham Science Centre, Abingdon, Oxfordshire, OX14 3DB, United Kingdom*
[2]*Department of Physics, University College Cork, Cork, Ireland*
[3]*General Atomics, P.O. Box, San Diego, California 92186-5608, USA*

(Received 3 February 2011; accepted 30 March 2011; published online 5 May 2011)

Deconvolution of Thomson scattering (TS) profiles is required when the gradient length of the electron temperature (T_e) or density (n_e) are comparable to the instrument function length (Δ_R). The most correct method for deconvolution to obtain underlying T_e and n_e profiles is by consideration of scattered signals. However, deconvolution at the scattered signal level is complex since it requires knowledge of all spectral and absolute calibration data. In this paper a simple technique is presented where only knowledge of the instrument function $I(r)$ and the measured profiles, $T_{e,\text{observed}}(r)$ and $n_{e,\text{observed}}(r)$, are required to obtain underlying $T_e(r)$ and $n_e(r)$. This method is appropriate for most TS systems and is particularly important where high spatial sampling is obtained relative to Δ_R. [doi:10.1063/1.3581230]

I. INTRODUCTION

Measurement of the H-mode transport barrier at the plasma edge plays a key role in understanding both stability and confinement. In relation to stability, the peak pressure gradient in the transport barrier determines the MHD stability to edge localized modes.[1] In relation to confinement, the width of the transport barrier determines the height at the top of the transport barrier and hence impacts on the plasma core parameters.[2] Scaling of the measured transport barrier widths from current devices is widely used to predict confinement of next step devices.[3] For these reasons it is important to diagnose the $T_e(r)$ and $n_e(r)$ transport barriers and hence the $p_e(r)$ transport barrier.

For some known instrument function $I(r)$, the underlying $n_e(r)$ may be recovered by fitting $n_e(r) \otimes I(r)$ to $n_{e,\text{observed}}(r)$ where $n_e(r)$ is described by some model. The n_e pedestal can be recovered by this method, since density is purely an intensity function. Temperature obtained from Thomson scattering (TS) is not an intensity function and so recovery of the T_e pedestal by deconvolution requires knowledge of the n_e pedestal. One widely used model for these profiles that captures the parameters of interest is the modified hyperbolic tangent (mtanh) function.[4] The mtanh function below, reproduced from Ref. 5, is used as the model for underlying T_e and n_e profiles throughout this paper.

$$\text{edge}(r;\vec{a}) = \frac{a_{\text{pedestal}} - a_{\text{sol}}}{2} \times \left[\text{mtanh}\left(\frac{a_{\text{etb}} - r}{2a_\Delta}, a_{\text{slope}}\right) + 1\right] + a_{\text{sol}} \quad (1)$$

$$\text{mtanh}(r', a_{\text{slope}}) = \left(\frac{(1 + a_{\text{slope}}r')e^{r'} - e^{-r'}}{e^{r'} + e^{-r'}}\right) \quad (2)$$

a_{pedestal} : pedestal height
a_{sol} : scrape off layer height
a_{etb} : transport barrier position
a_Δ : transport barrier width
a_{slope} : core slope

The intensity weighting of the temperature profile by the density profile is illustrated in Fig. 1. The observed T_e and n_e profiles are obtained by considering the scattered signals measured by a four channel spectrometer with spectral transmission shown in Fig. 2. The scattered signals are determined by considering the $T_e(r)$ and $n_e(r)$ variation within the radial instrument function I(r) shown and fitting the spectra from each $I(r)$ with a single T_e and n_e. An assumption of a single T_e and n_e within a scattering length is implied by a TS fit to a spatial point. The simple convolutions of $n_e(r) \otimes I(r)$ and $T_e(r) \otimes I(r)$ are also shown in Fig. 1. The observed density pedestal matches $n_e(r) \otimes I(r)$ well and hence may be recovered by forward convolution. The observed temperature pedestal does not match $T_e(r) \otimes I(r)$ and hence is not recoverable by a similar forward convolution. This occurs as the temperature pedestal is weighted outwards by the density pedestal.

Although a filter spectrometer is used for calculations performed in this paper, the effects considered here are generic to all Thomson scattering systems. However, these effects are dependent on the spectral range covered by the spectrometer. The detailed effects for systems measuring only below and both below and above the laser wavelength will differ.

In the following sections of this paper a technique for fitting directly to measured scattered signals, originally outlined in Ref. 6, is described. In subsequent sections, a deconvolution technique for the temperature pedestal that requires

a)Electronic mail: rory.scannell@ccfe.ac.uk.
b)Present address: ITER Organisation, Diagnostics Division, Cadarache, 13106, St. Paul-lez-Durance, France.

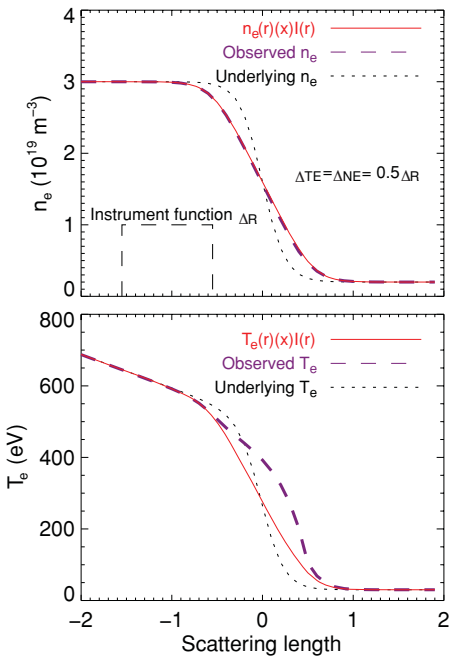

FIG. 1. (Color online) Black dotted line shows underlying $T_e(r)$ and $n_e(r)$ profiles. Red continuous line shows simple convolution of the underlying profiles with the instrument function Δ_R. The purple dashed line shows the observed T_e and n_e profiles obtained from refitting at high spatial sampling to scattered signals observed with an instrument function Δ_R. The refitting is performed with no knowledge of the instrument function.

consideration of $T_{e,\text{observed}}(r)$, $n_{e,\text{observed}}(r)$, and $I(r)$ but not the observed scattered signals is described. This technique is more straightforward to implement and produces similar pedestal parameters within certain constraints. The influence of instrument function uncertainty and noise in the data on the deconvolution process are also considered.

II. SIGNAL FITTING METHOD

The following section describes methods to fit radial models of $T_e(r)$ and $n_e(r)$, both to observed $T_e(r)$ and $n_e(r)$ and to observed scattered signals. A flow diagram in Fig. 3 shows how observed data are obtained from the scattering process. The flow diagram also shows the operation of the two fitting methods.

The temperature and density profiles in the plasma give rise to a Thomson scattered spectrum as a function of radius

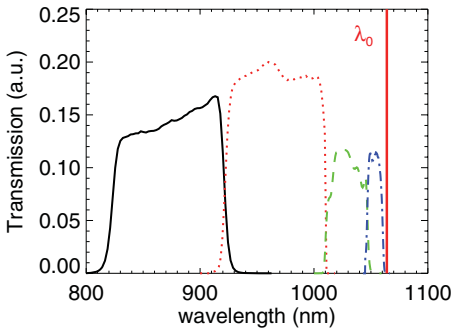

FIG. 2. (Color online) Spectral transmission of polychromator channels.

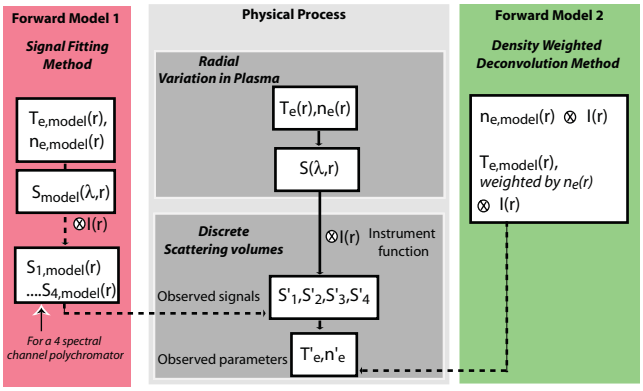

FIG. 3. (Color online) Schematic of the different fitting techniques used in the paper. Forward model 1 fits to the observed scattered signals. Forward model 2 fits to the observed temperature and density.

and wavelength:

$$[C_{\text{geom}} E_{\text{laser}} \sigma_{\text{TS}}] n_e(r) S_{\text{TS}}(\lambda, T_e(r), \theta)) \rightarrow S(\lambda, r), \tag{3}$$

where C_{geom} is a geometry factor, taking into account scattering length and solid angle, E_{laser} is the laser energy, and σ_{TS} is the Thomson scattering cross section. S_{TS} is the Thomson scattering spectrum as described by Selden[7] and $S(\lambda, r)$ is the resulting scattered spectrum as determined by the radially varying profiles of temperature and density.

The process of observing discrete scattered signals in some radial bin involves spatial convolution of the scattered signals by the radial instrument function $I(r)$ over some scattering length Δ_R and integration of the scattered spectrum in discrete spectral bins of transmission $\phi(\lambda)$:

$$[C_{\text{geom}} E_{\text{laser}} \sigma_{\text{TS}}] \int_{-\Delta_R/2}^{\Delta_R/2} n_e(r) I(r) \times \int_0^{\infty} \Phi(\lambda) S_{\text{TS}}(\lambda, T_e(r), \theta) d\lambda dr \rightarrow S_{\text{observed}}(\lambda, r). \tag{4}$$

The observed scattered signals are then fitted giving rise to observed temperature and density profiles:

$$S_{\text{observed}}(\lambda, r) \rightarrow T_{e,\text{observed}}(r), n_{e,\text{observed}}(r). \tag{5}$$

The typical deconvolution technique works by convolving models of underlying n_e and T_e by the instrument and fitting this to the observed n_e and T_e profiles. This forward fitting process is described by the equations below:

$$\{n_{e,\text{model}}(r) \otimes I(r) \Leftrightarrow n_{e,\text{observed}}(r)\} \rightarrow n_e(r), \tag{6}$$

$$\{T_{e,\text{model}}(r) \otimes I(r) \Leftrightarrow T_{e,\text{observed}}(r)\} \rightarrow T_e(r). \tag{7}$$

Where the forward convolution is represented by $\{\Leftrightarrow\}$. Rather than fitting to observed temperature and density profiles, it is possible to fit to observed scattered signals instead. The advantage of fitting at the signal level is that the convolution may be taken into account at the signal level, where

the convolution actually occurs, and hence will result in the correctly deconvolved temperature pedestal. A further advantage is that fitting at the signal level removes the systematic error from performing a T_e,n_e fit at each point individually. The process of signal fitting may be described as:

$$\{[(T_{e,\mathrm{model}}(r), n_{e,\mathrm{model}}(r)) \rightarrow [\mathrm{Eq.}\,(4)] \rightarrow S_{\mathrm{model}}(\lambda, r)] \Leftrightarrow S_{\mathrm{observed}}(\lambda, r)\} \rightarrow n_e(r), T_e(r). \tag{8}$$

This then results in direct recovery of the underlying profiles. The disadvantage of this technique is that it requires all of the absolute and spectral calibration information for each spectrometer at each step of the process. Although only Thomson scattered signals are considered in this paper, data from other diagnostics could be included to constrain the TS data as in Ref. 8.

III. DENSITY WEIGHTED DECONVOLUTION METHOD

A. A scattering length with flat T_e and flat n_e

The assumption of constant n_e and T_e in a scattering length is implicit in performing a TS fit to that point. This assumption is valid for short scattering lengths and in the plasma core where no large gradient exists. However, at the plasma edge this assumption is not valid due to steep gradients.

The impact of measuring about a step function in n_e and T_e is shown in Fig. 4. In this example the core plasma has an electron density of 4×10^{19} m^{-3} and an electron temperature of 1 keV, the scrape off layer has zero density. Three scattering lengths are considered, whose radial measurement locations are shown in Fig. 4(a) and observed scattered spectra are shown in Fig. 4(b). A scattering length fully inside the plasma edge measures $n_e = 4 \times 10^{19}$ m^{-3} and $T_e = 1$ keV. A second scattering length centered at the plasma edge measures $n_e = 2 \times 10^{19}$ m^{-3} and $T_e = 1$ keV. A third scattering length, 90% outside the plasma edge, measures $n_e = 0.4 \times 10^{19}$ m^{-3} and $T_e = 1$ keV. In general for the case considered, if the scattering length is partially inside the plasma, a core plasma electron temperature will be measured and recorded at the position of the scattering center. The observed radial profile from any arbitrary scattering center is shown in Fig. 4(c) for the same underlying T_e and n_e profiles.

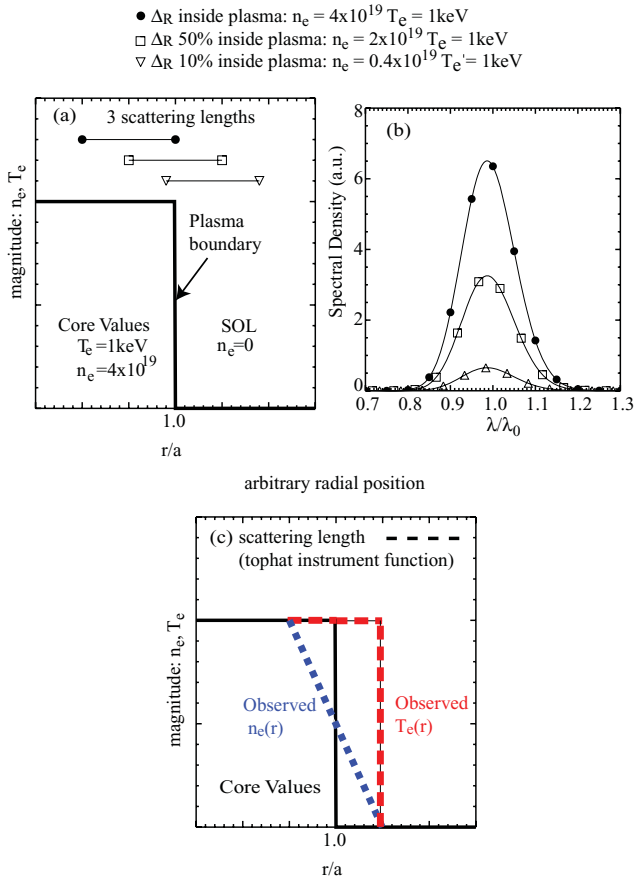

FIG. 4. (Color online) Effect of variation of scattering length position on the measurement of T_e and n_e. For illustrative purposes a plasma with constant core T_e and n_e and zero scrape off layer n_e are used. (a) Measurement positions of three scattering lengths about the step functions in T_e and n_e. (b) Spectra observed by the three scattering length shown in (a), where λ_0 is the laser wavelength. (c) Temperature and density observed for arbitrary scattering length position.

B. A scattering length with T_e gradient and flat n_e

The shape of the Thomson scattering spectrum is determined by the electron temperature and scattering angle θ. In the low temperature approximation the width of a measured Thomson scattering spectrum, $\Delta\lambda_{\mathrm{width}}$, is proportional to the square root of the temperature:

$$\frac{\Delta\lambda_{\mathrm{width}}}{\lambda_0} = \frac{2\sin(\theta/2)}{c}\sqrt{\frac{2k_bT_e}{m_e}} \tag{9}$$

also at low temperature, the blue-shifted peak of the spectrum from the laser wavelength, $\Delta\lambda_{\mathrm{blueshift}}$, relates to its temperature[9] as:

$$\frac{\Delta\lambda_{\mathrm{blueshift}}}{\lambda_0} \approx -2.8x10^{-5}T_e(eV)\sin^2(\theta/2). \tag{10}$$

The variation with electron temperature of the width and blueshifted peak of the Thomson scattering spectrum as calculated from the spectrum obtained from Ref. 7 and modified by Ref. 10 normalized to laser wavelength are shown in Fig. 5. If there is temperature variation within a scattering length, the peak of the measured TS spectrum will approximately equal the mean peak of all the spectra within the scattering length. Assuming the peak position of the spectrum is the main factor in determining the electron temperature, then for an instrument function I(r), the observed temperature will be the instrument function weighted sum of all the temperatures within the scattering length:

$$T_{e,\mathrm{observed}} \approx \frac{\int T_e(r)I(r)dr}{\int I(r)dr}. \tag{11}$$

The width of the observed spectrum will approximately equal the mean width of all the spectra within the scattering length. This is the case because the addition of Gaussians with

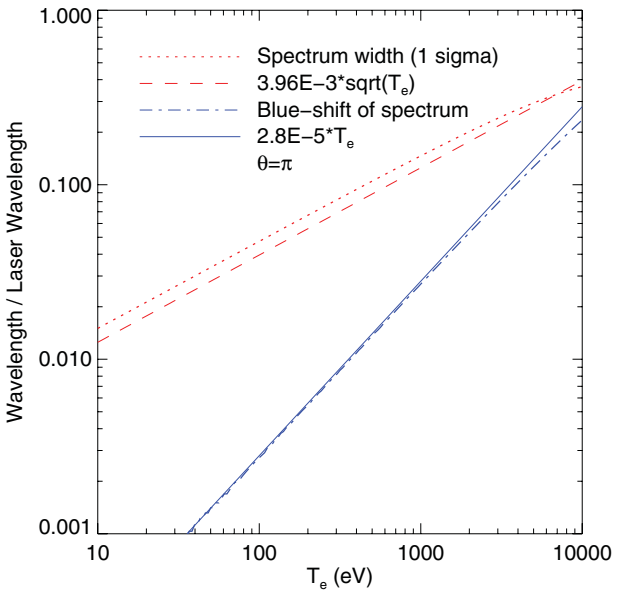

FIG. 5. (Color online) Variation of the blueshifted peak and width of the Thomson scattered spectrum with electron temperature and comparison with their low temperature approximations. The approximations from Eqs. (9) and (10) and the actual values, as determined from the fully relativistic spectrum, are shown.

the same intensities and similar widths produces a Gaussian of width approximately equal to the mean width of the added Gaussians. The impact of this on measured temperature may be understood by considering the following case. If the temperature varies from $T_{e,1}$ to $T_{e,2}$ across a scattering length, resulting in the spectral width varying from $\Delta\lambda_1$ to $\Delta\lambda_2$, the measured width will approximate to:

$$\Delta\lambda_{\text{observed}} \approx \frac{\Delta\lambda_1 + \Delta\lambda_2}{2} \tag{12}$$

and assuming the temperature is determined by the width of the scattered spectrum, as in Eq. (9), the observed temperature will be given by:

$$T_{e,\text{observed}} \propto \frac{1}{4}(\Delta\lambda_1 + \Delta\lambda_2)^2 \tag{13}$$

and hence

$$T_{e,\text{observed}} \propto \frac{1}{4}(\sqrt{T_{e,1}} + \sqrt{T_{e,2}})^2 \tag{14}$$

or more generally the observed temperature from a scattering length with constant density will be given by

$$T_{e,\text{observed}} \approx \left(\frac{\int \sqrt{T_e(r)} I(r) dr}{\int I(r) dr}\right)^2. \tag{15}$$

Both Eqs. (11) and (15) are approximations as T_e is not determined uniquely by the width of the spectrum or the blueshift. In reality the determination of T_e is more complex and uses the full information represented by the shape of the spectrum.

C. A scattering length with T_e and n_e gradient

If there is an n_e variation within the scattering length, the observed density will be very close to the convolution of the underlying density profile and the instrument function $I(r)$.

$$n_{e,\text{observed}} = \frac{\int n_e(r) I(r) dr}{\int I(r) dr} \tag{16}$$

Due to the n_e variation, the measured T_e is weighted to the high n_e region. Since the T_e converged is then incorrect, the n_e will also be incorrect. The density error is only a second order effect and is typically small for practical purposes. Modifying Eq. (11) to take into account the density variation within the scattering length, the weighted temperature will be given by

$$T_{e,\text{observed}} = \frac{\int T_e(r) n_e(r) I(r) dr}{\int n_e(r) I(r) dr}. \tag{17}$$

An alternative density weighted temperature could be obtained from Eq. (15), assuming the width of the spectrum is the dominant factor:

$$T_{e,\text{observed}} = \left(\frac{\int \sqrt{T_e(r)} n_e(r) I(r) dr}{\int n_e(r) I(r) dr}\right)^2. \tag{18}$$

D. Application to pedestal

While Eq. (17) applies to the measurements from an individual scattering length, the equivalent for a radial profile of temperature is a convolution operation and is given by

$$T_{e,\text{observed}}(r) = \frac{(T_e(r) n_e(r)) \otimes I(r)}{n_e(r) \otimes I(r)}. \tag{19}$$

Similarly the equivalent radial profile for Eq. (18) is

$$T_{e,\text{observed}}(r) = \left(\frac{(\sqrt{T_e(r)} n_e(r)) \otimes I(r)}{n_e(r) \otimes I(r)}\right)^2. \tag{20}$$

Observed radial profiles of temperature and profiles obtained from application of Eqs. (19) and (20) are shown in Fig. 6. In this figure the top two panels show the underlying density profiles and instrument functions. The $T_e(r)$ profiles in the center two panels show that both Eqs. (19) and (20) produce $T_e(r)$ profiles very close to the observed radial profile of temperature and hence can be used in forward convolution of the temperature profile. The bottom two panels of Fig. 6 show the difference between the underlying temperature profile and the determined and observed temperature profiles. These profiles show that although this method provides a good approximation to the determined temperature profiles, it is not exact and hence there will be systematic deviations in measured pedestal parameters. These

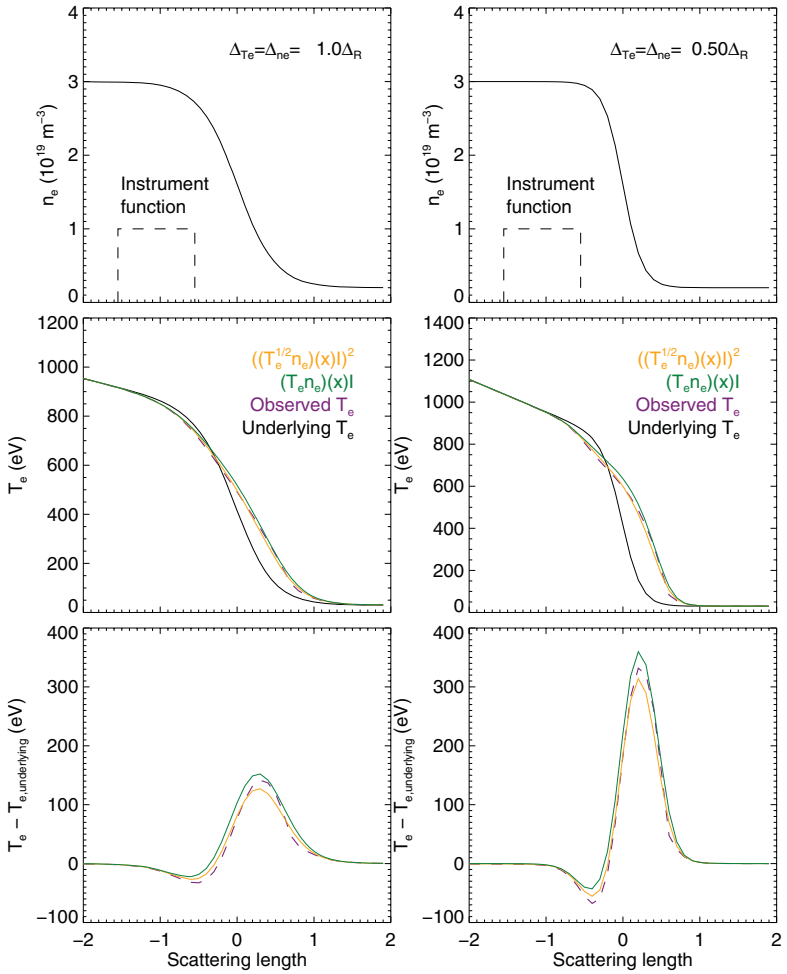

FIG. 6. (Color online) To deconvolve the temperature pedestal by forward deconvolution an approximation to the observed temperature profile is required. Here two approximation techniques, n_e weighting of T_e and $\sqrt{T_e}$, are compared. The left column examines pedestal widths of $\Delta_{Te} = \Delta_{ne} = \Delta_R$ and the right column examines widths of $\Delta_{Te} = \Delta_{ne} = 0.5 * \Delta_R$.

systematic errors will become greater as the pedestal width becomes narrower.

IV. SYSTEMATIC ERRORS IN OBSERVED PEDESTAL PARAMETERS DUE TO DECONVOLUTION

Application of various deconvolution techniques to the pedestal is shown in Fig. 7. The observed pedestal is determined by considering the radial variation of scattered signals within the scattering length Δ_R and refitting for temperature and density at a spatial sampling of $0.1*\Delta_R$. The pedestal width was then varied as a fraction of the scattering length, while maintaining $\Delta_{ne} = \Delta_{Te}$ and maintaining the same transport barrier position for both pedestals. No errors are added to the signals and hence the deviation of observed parameters from underlying in Fig. 7 are systematic due to the actual convolution occurring at the signal level and forward convolution approximations at the T_e, n_e level.

The results for the density pedestal show that the transport barrier position and pedestal height may be recovered without consideration of an instrument function. The density pedestal width will be overestimated without knowledge of the instrument function. The narrower the pedestal the greater the relative overestimate in the observed pedestal width. Figure 7(a) shows the pedestal width is recovered well using forward convolution by the instrument function. The width is not exactly recovered at narrow pedestal widths as the mean density in a scattering volume is not exactly recovered due to T_e variation within the scattering length.

The shaded region in Fig. 7(a) shows the uncertainty in the recovered Δ_{ne} due to an uncertainty of $\pm 10\%$ in the width of Δ_R. At an underlying pedestal width of $0.5*\Delta_R$ an uncertainty in the instrument function of $0.1\Delta_R$ results in a $\pm 20\%$ uncertainty measuring Δ_{ne}. The width of the instrument function for TS measurements is determined both by the interaction of the width of the laser beam and the image of a finite collection volume created by the collection optics, both of which are difficult to measure with high accuracy.

Fitting to $T_{e,\mathrm{observed}}(r)$ with no instrument function results in the observed temperature pedestal height being underestimated and transport barrier position measured outside of its actual location as shown in Fig. 7 panels (e) and (f). This occurs since the temperature pedestal is weighted outward by the density pedestal and the pedestal height falls due to averaging with the low temperature scrape off layer. These effects may be understood by examination of the observed profiles in

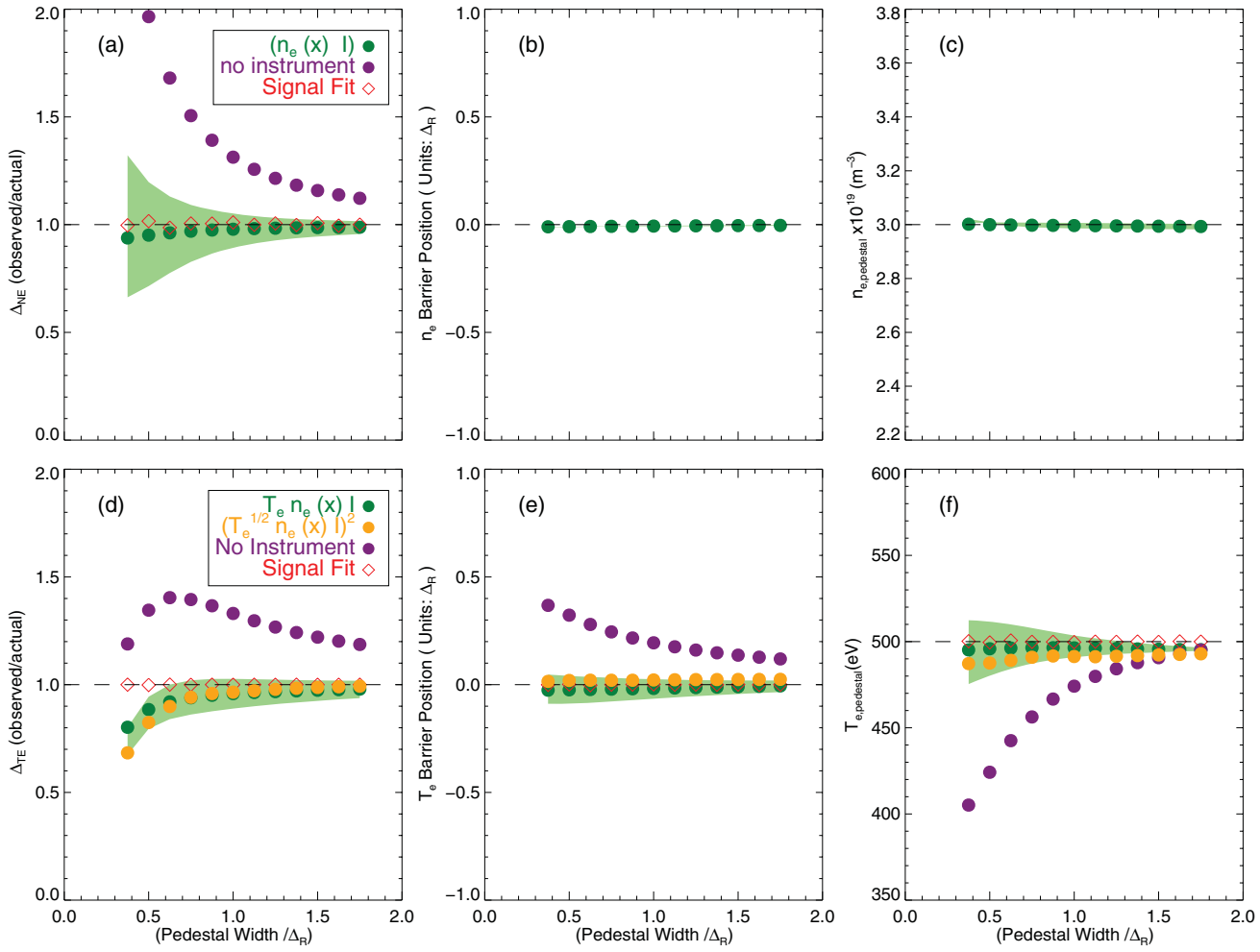

FIG. 7. (Color online) The application of various forward models to recover the underlying pedestals from observed data is compared. The recovered values of pedestal width, transport barrier position, and pedestal height are shown for electron density in the top three panels and electron temperature in the bottom three panels. The dashed horizontal line in each panel shows the underlying pedestal value. The x-axis is the ratio of underlying temperature and density pedestal width to instrument function width, in all cases $\Delta_{Te} = \Delta_{ne}$.

Fig. 6. The width of the temperature pedestal is overestimated without consideration of the instrument function.

The observed temperature pedestal width is increasingly not well approximated by the deconvolution techniques for smaller Δ_{Te}/Δ_R. At $\Delta_{Te}/\Delta_R = 0.5$ the measured pedestal width is underestimated by ≈25%. This underestimate occurs because the weighted deconvolution techniques for the temperature pedestal are approximations as may be seen from Fig. 6. The measured temperature pedestal parameters do not vary significantly depending on whether deconvolution is performed by Eq. (19) or (20). The pedestal width is recovered more accurately by Eq. (19) at low Δ_{Te}/Δ_R, however the transport barrier position is recovered more accurately by Eq. (20).

V. ROLE OF RANDOM ERROR

The process of deconvolution is sensitive to noise. Figure 8 shows underlying T_e and n_e profiles (dotted black), simulated measurements at discrete radial bins (circles), and profiles recovered from forward fitting (dashed green and continuous green). The simulated T_e and n_e data have error added due to the finite numbers of detected photons; the TS system used has an etendue of 0.3 mm^2sr from each spatial point, a laser energy of 1 J, optical transmission of 40% and a peak effective quantum efficiency of 10%. Background light is calculated from bremsstrahlung emission from a plasma of peak temperature 2 keV integrating over a path length of 1 m, in addition to this a fixed detector noise (or readout noise) of 200 photoelectrons is assumed for each measurement. These uncertainties combine to produce a random error in n_e of ≈3% at 3E19 m^{-3} and ≈25% at 2E18 m^{-3}.

Observed pedestal widths are shown in Fig. 9 for 20 iterations of this Monte Carlo code for underlying pedestal widths of $0.25\Delta_R$, $0.5\Delta_R$, Δ_R, and $2\Delta_R$. The results show, as expected, that narrower pedestal widths result in a large variation in the observed pedestal width. It is also shown that the temperature pedestal width is significantly more difficult to determine than the density pedestal width. However, it is still possible to recover pedestal widths narrower than the instrument function provided the measurement error is low enough.

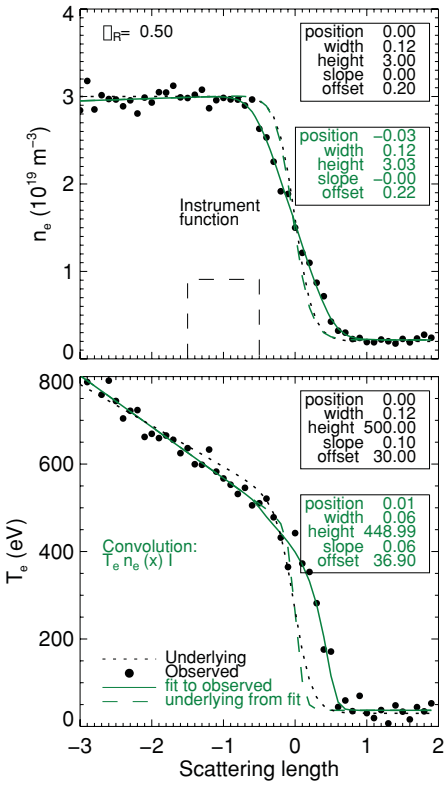

FIG. 8. (Color online) Fit to simulated data showing the recovery of a pedestal. The underlying pedestal is shown, from which discrete T_e and n_e are observed (circles). The fit to this observed data using the forward convolution models is shown, as well as the underlying profiles implied by the fit. The ratio of pedestal width to instrument function, $\Delta_{Te,ne}/\Delta_R$, is ≈ 0.5 hence full deconvolution is important.

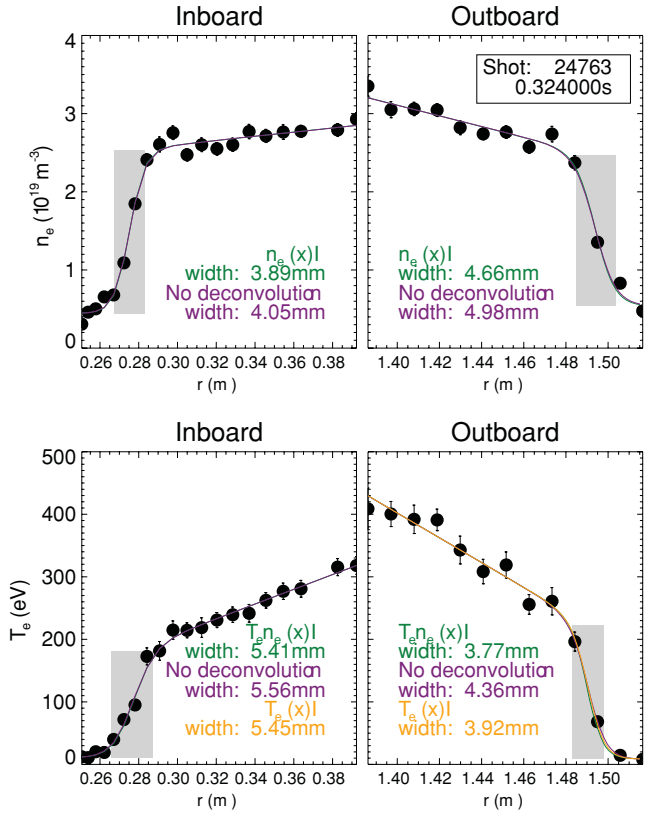

FIG. 10. (Color online) Fits to the inboard and outboard pedestals obtained from a single timeslice during a MAST pulse. The width numbers shown are the fitted parameter, the grayed areas represent the full pedestal width (4 times the fitted parameter). The instrument function at the inboard transport barrier is $\Delta_R \approx 5$ mm, hence $\Delta_{Te,ne}/\Delta_R \approx 4$, the instrument function at the outboard transport barrier is $\Delta_R \approx 10$ mm, hence $\Delta_{Te,ne}/\Delta_R \approx 1.5$.

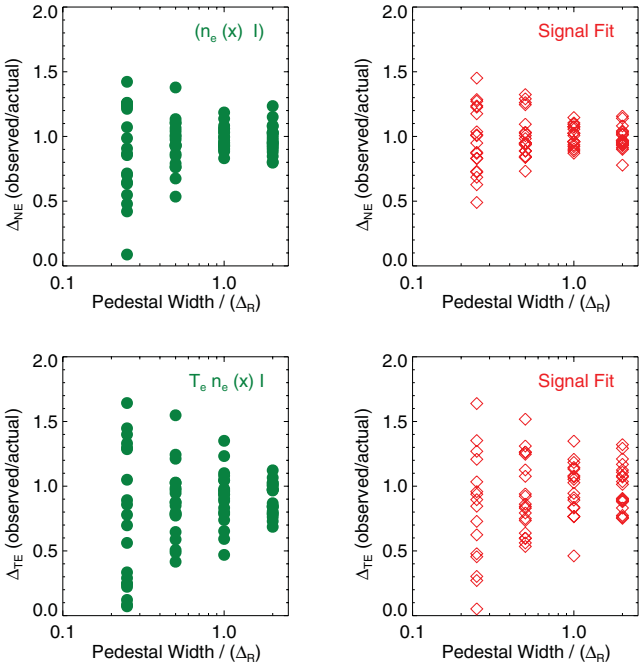

FIG. 9. (Color online) Y-linear X-log plot. Effects of adding noise (Monte Carlo analysis) to measured data and refitting pedestals using the deconvolution techniques indicated. The pedestal widths obtained, Δ_{Te} and Δ_{ne}, are examined for $\Delta_{Te} = \Delta_{ne} = 0.25{*}\Delta_R$, $0.5{*}\Delta_R$, Δ_R and $2{*}\Delta_R$.

A comparison of deconvolution at the signal level and deconvolution at the n_e and T_e level is shown in Fig. 9. For forward deconvolution using the $n_e(r) \otimes I(r)$ and $T_e(r)n_e(r) \otimes I(r)$ approximations the uncertainty due to noise is larger than that due to systematic error from the convolution approximation. Since a similar range of pedestal widths is recovered using the signal fitting technique, in this case there is little benefit to fitting at the signal level. In general, where noise due to random error dominates that due to the systematic uncertainty due to the convolution approximations, there is no benefit to fitting at the signal level. Where random error is low, due to good photon statistics or averaging over a large number of timeslices, it is possible to recover very narrow pedestal widths using the signal fitting method.

Pedestals observed during MAST shot 24763 at 0.324 s are shown in Fig. 10. In this example density and temperature pedestals are fitted to data taken from both the inboard, close to the center column, and outboard sides of the plasma. For the MAST TS system, the instrument function at the inboard side has a width of $\Delta_R \approx 5$ mm, and at the outboard side has a width of $\Delta_R \approx 10$ mm. The underlying density pedestal is obtained by two techniques: fitting directly to observed data with no instrument function and fitting including an instrument function convolution. The underlying temperature pedestal is obtained by three techniques: no deconvolution, convo-

lution with the instrument function, and density weighted convolution.

At the inboard side the observed pedestals widths are $\Delta_{Te,ne} \approx 20$ mm (four times the fitted parameter shown on the plots) and are much broader than the instrument function resulting in a width to resolution ratio of $\Delta_{Te,ne}/\Delta_R \approx 4$. At $\Delta_{Te,ne}/\Delta_R \approx 4$ deconvolution has little impact on the observed pedestal widths. At the outboard side the observed pedestal widths of $\Delta_{Te,ne} \approx 16$ mm are comparable to the instrument function, having a width to resolution ratio of $\Delta_{Te,ne}/\Delta_R \approx 1.6$, and hence deconvolution has a significant impact on the widths observed. At narrower pedestal widths of down to $\Delta_{Te,ne} = 5$ mm, as have been observed on MAST[11], the method of deconvolution becomes increasingly important.

VI. CONCLUSION

Fitting without deconvolution to the observed TS T_e pedestal results in significant systematic errors in the pedestal width, height, and position. Two methods are discussed in this paper to better recover the underlying T_e pedestal. Using these methods is particularly important where pedestal width is similar in size to the instrument function, but is required even where the pedestal widths are larger than the instrument function. For example, for a pedestal width twice as large as the instrument function an $\approx 20\%$ error would be obtained in the observed Δ_{Te} without deconvolution.

One method considered is *density weighted deconvolution*. This method deconvolves from the observed temperature measurements using the known instrument function and the underlying density pedestal, where the density pedestal is recovered separately. This is a practical and easy to implement solution as it does not require all of the calibration information from each radial point. Two density weighting functions for the temperature profile were considered, one based on the weighted temperature within an instrument function and the other based on the weighted square root of the temperature. The two weighting functions were found to produce similar results. However, deconvolution at the n_e, T_e level is only an approximation and at narrow pedestal widths, less than approximately half the instrument function, the systematic error between the observed and the actual pedestal width becomes significant.

To recover narrow pedestal widths with no systematic error a second deconvolution method, the *signal fitting method*, based on fitting directly to these observed signals is described. The advantage of this method is that it has no systematic error as it represents exactly what is happening in the system. The disadvantage is that it is more difficult to implement, as the full model for the system including all absolute and spectral calibration information is required.

A further factor to consider in determining which deconvolution method to use is the uncertainty on the recovered temperature pedestal. At narrow pedestal widths any derived information can only be treated with confidence if the instrument function is well known and noise is low. Both of these factors will influence the signal fitting method and intensity weighted temperature pedestal deconvolution method in a similar manner. If measurement error is dominated by uncertainty due to either of these factors, then the easier to implement instrument weighted method is sufficient.

ACKNOWLEDGMENTS

This work was funded partly by the RCUK Energy Programme under Grant EP/I501045 and the European Communities under the contract of Association between EURATOM and CCFE. The views and opinions expressed herein do not necessarily reflect those of the European Commission. This work was carried out within the framework of the European Fusion Development Agreement.

NOMENCLATURE

$T_e(r)$	Underlying T_e profile
$n_e(r)$	Underlying n_e profile
$I(r)$	Radial instrument function
$T_{e,\mathrm{observed}}(\mathrm{r})$	Measured T_e profile
$n_{e,\mathrm{observed}}(r)$	Measured n_e profile
Δ_{Te}	Underlying T_e pedestal width
Δ_{ne}	Underlying n_e pedestal width
Δ_R	Scattering length (equal to the width of the instrument function)
$S(r, \lambda)$	Radial variation of the Thomson scattered spectrum
θ	Scattering angle
λ_0	Laser wavelength

[1]H. R. Wilson, P. B. Snyder, G. T. A. Huysmans, and R. L. Miller, Phys. Plasmas **9**, 1277 (2002).
[2]E. J. Doyle *et al.*, Nucl. Fusion **47**, S18 (2007).
[3]M. N. A. Beurskens *et al.*, Plasma Phys. Controlled Fusion **51**, 124051 (2009).
[4]R. J. Groebener and T. N. Carlstrom Plasma Phys. Controlled Fusion **40**, 673 (1998).
[5]E. Arends, "Density gradients in spherical tokamak plasmas," Ph.D. thesis (Technische Universiteit Eindhoven, 2003).
[6]R. Scannell, M. Walsh, P. G. Carolan, N. J. Conway, A. C. Darke, M. R. Dunstan, D. Hare, and S. L. Prunty, Rev. Sci. Instrum. **77**, 10E510 (2006).
[7]A. C. Selden, Phys. Lett. **79A**, 405 (1972).
[8]R. Fischer, A. Dinklage, and E. Pasch, Plasma Phys. Controlled Fusion **45**, 1095 (2003).
[9]J. Sheffield, Plasma Phys. **14**, 783 (1972).
[10]O. Naito, H. Yoshida, and T. Matoba, Phys. Fluids B **5**, 4256 (1993).
[11]A. Kirk, T. O'Gorman, S. Saarelma, R. Scannell, H. R. Wilson1, and the MAST team, Plasma Phys. Controlled Fusion **51**, 065016 (2009).